

Supplementary information file

Voltage-activated transport of ions through single-walled carbon nanotubes

Khadija Yazda¹, Saïd Tahir¹, Thierry Michel¹, Bastien Loubet², Manoel Manghi², Jeremy Bentin³, Fabien Picaud³, John Palmeri¹, François Henn¹, Vincent Jourdain^{1,*}

¹Laboratoire Charles Coulomb, UMR 5221 CNRS-Université de Montpellier, Place Bataillon, 34095 Montpellier Cedex 5, France; ²Laboratoire de physique théorique (IRSAMC) UMR 5152 CNRS-UPS, Université de Toulouse, France; ³Laboratoire de Nanomédecine Imagerie et Thérapeutique (NIT), EA4662 Université de Bourgogne Franche-Comté, UFR ST & CHU Médecine, France

* Contact: vincent.jourdain@umontpellier.fr

1) Raman characterization of the structural distribution of the SWCNTs

The structural distribution (diameter distribution) of the CNTs used for the fluidic devices was evaluated from Raman analysis on different samples all grown in the same CCVD conditions (lattice-oriented growth). The diameter distribution shown in S1a was obtained from the RBM recorded for 95 different tubes using 532 nm and 633 nm wavelengths and was calculated using the relationship $\omega_{RBM} (cm^{-1}) = (235.9/d_d) + 5.5$ which was validated for SWCNTs on thermal SiO₂ [1]. The nanotube diameters were found to range between 1.2 and 2 nm with most of tubes at 1.3-1.5 nm. Most SWCNTs were found to display a G-band profile characteristic of semiconducting nanotubes.

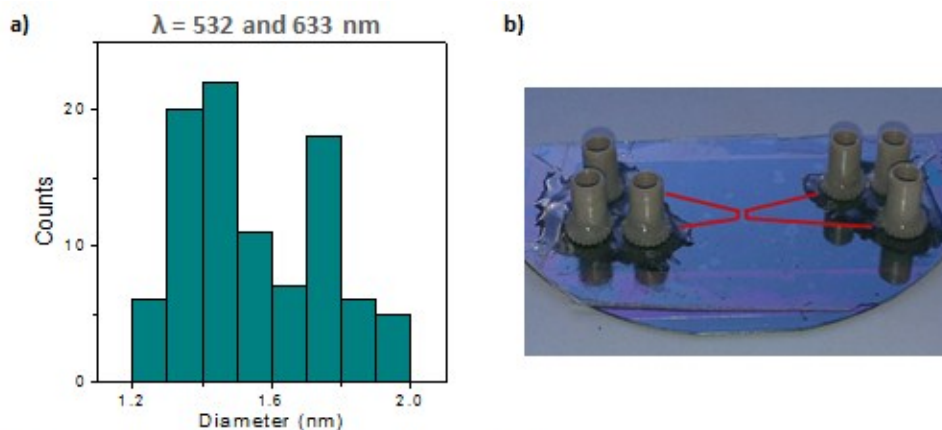


Figure S1: (a) Diameter distribution of the carbon nanotubes used for the microfluidic device fabrication (b) Picture of a CNT-based microfluidic device used for the ionic transport studies.

2) Raman characterization of the doping and strain along SWCNTs under and outside SU-8

Raman characterizations of CNTs covered by a photoreticulated SU-8 layer were carried out on different samples that differ by the SU-8 wall dimensions and UV exposure conditions. These samples were neither submitted to the oxygen plasma treatment, nor sealed by a NOA layer. Thus the CNTs in these samples are partially covered by a top SU-8 layer. Raman mapping of the tubes crossing the SU-8 walls were recorded outside and below the wall. Note that all the tube sections (both outside and below the wall) have been exposed to SU-8 during the channel creation step. The nanotube sections outside the wall were temporarily exposed to unreticulated SU-8 while the sections below the wall were exposed to UV during the lithography step and are consequently covered with a reticulated layer of SU-8. G-band mapping of the different samples showed significant fluctuations of the G-band frequency (ω_G) along the tubes which were more pronounced for the tubes under the SU-8 matrix. The level and the spatial correlation of these fluctuations were observed to vary from one sample to another depending on the fabrication conditions of each sample. Four different cases were observed: 1) a double line feature observed for all the tubes under SU-8 where the G-band is upshifted in these lines compared to the other regions of the same tube (figure 4a of the main text); 2) local G-band shifts without spatial correlation between neighboring tubes (figure S2a); 3) negligible G-band shifts along the tubes under SU-8 (figure S2b); 4) a double-line feature for all the tubes under SU-8 where the G-band is downshifted in these lines compared to the other positions along the tube (figure S2c).

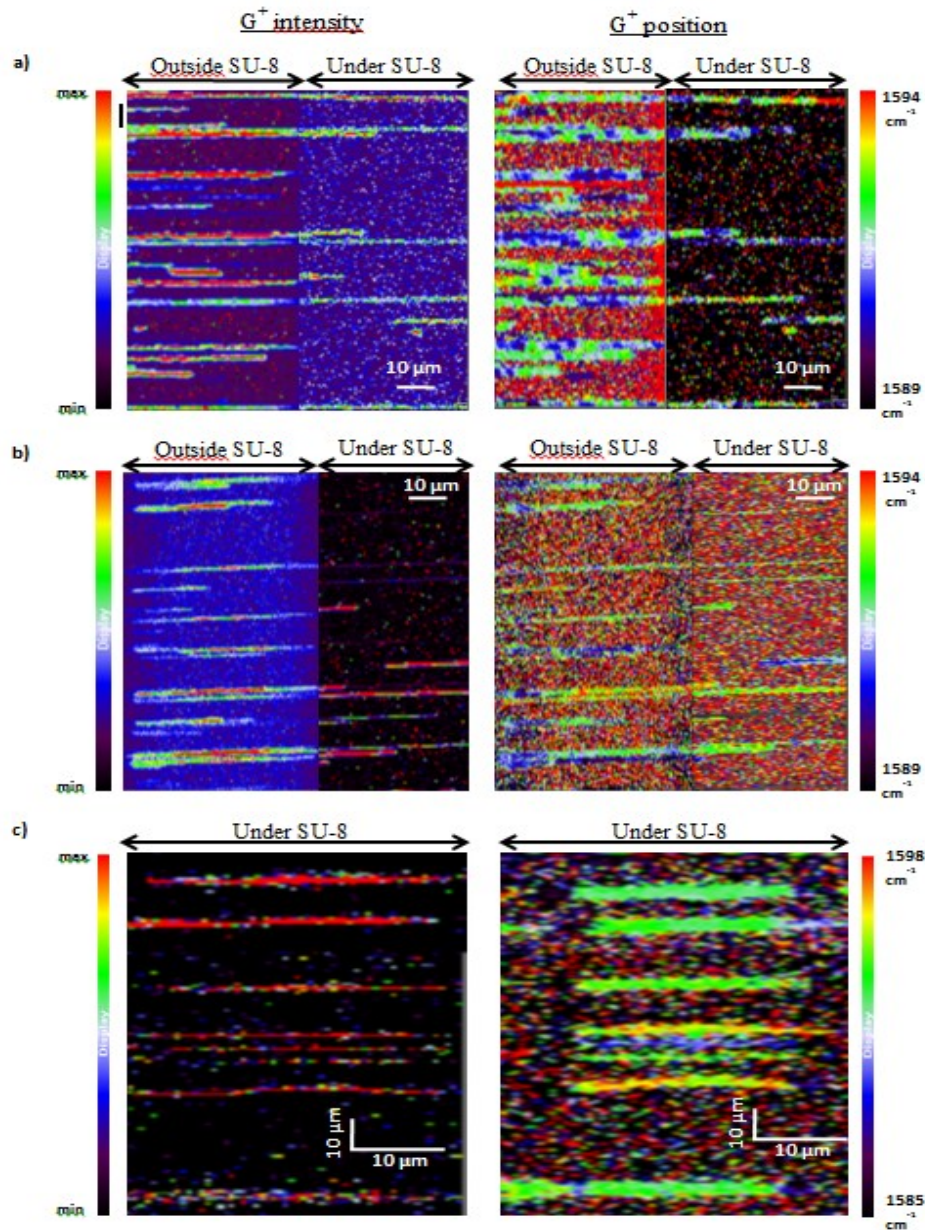


Figure S2: Raman maps of CNTs embedded in SU-8 matrix displaying the variation in intensity (left) and frequency (right) of the G-band along the tubes outside and below the SU-8 wall. (a) sample displaying local G^+ shifts of $5\text{-}6\text{ cm}^{-1}$, (b) sample with no significant shifts of $2\text{-}3\text{ cm}^{-1}$, (c) sample showing important shifts $4\text{-}5\text{ cm}^{-1}$ and double line spatial correlation for all the tubes under SU-8.

3) MD simulation protocol

The system was composed of a periodic carbon nanotube of length 10 nm and diameter 1.4 nm for a total number of carbon atom equal to 1640. The nanotube was a $(n,m) = (10,10)$ following Hamada notation. It was charged homogenously with a negative surface charge density of 0.038

C/m², distributed on the carbon atoms of the nanotube. The defect charge nanotube presented a central part which was neutral while the other atoms kept their initial charge value.

All the systems were completely hydrated with 207 water molecules and counter ions were added to the solution in order to compensate the nanotube charge. For the homogeneously charged nanotube, 10 potassium ions were added while only 8 were used in the case of the defect charge nanotube.

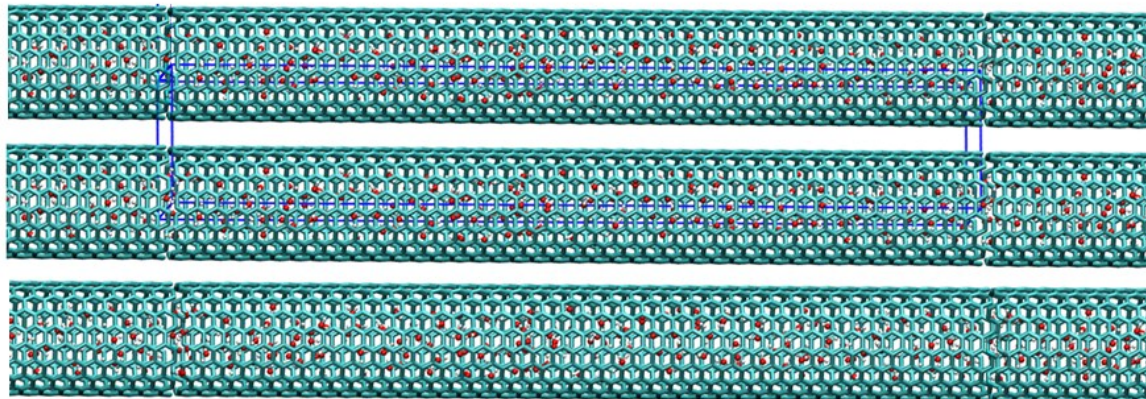


Figure S3: the simulated system is made of one (10,10) carbon nanotube (here the homogeneously charged nanotube) repeated in the three space directions according to the blue parallelepiped of dimension (1.68 nm; 1.68 nm; 10.19 nm). Only 2 cells were repeated in the tube axis direction and in the perpendicular axis direction for clarity.

Parameters for the atoms were taken from the CHARMM27 force field [2], well suited for the use of small aromatic molecules. The TIP3P [3] model for water molecules was used. Note that Ganjiani *et al.* [4] showed that the Lennard-Jones parameters describing the pair interaction between carbon atoms and water molecules influenced the hydrophobicity of the CNT. Many approaches dealt with the particular organization of the water layer inside confined hydrophobic nanotube. These layers present mostly oscillatory density profile which could be at the origin of selective properties of the nanopore [5, 6, 7, 8]. This layer organization could be modified depending on the water model and the conduction mode could be also changed depending on the simulation model [9]. For example, TIP3P model lead to faster diffusive conduction of the separated water molecules compared to TIP4P/2005 model which implied a slower conduction due to the formation of small water cluster in confined conditions [10]. Nevertheless, the different modes of conduction were not demonstrated experimentally and were only the consequences of the chosen model. The influence of polarizable water on the ion organization in confined system was also implemented. The inclusion of polarizability quantitatively affects the hydrogen bond network, and thus could impact the properties of confined water molecules. Indeed, tighter hydrogen bonds and thus shorter distance between neighbors are observed when polarizable water model is used. This involves a decrease of the diffusion coefficient [11]. The organization of the ions could thus be impacted by these properties since it depends on the water model. In particular, it has been shown that hydronium attraction to the surface was due to the neglect of polarizability and that the movement of hydroxide to the surface did not pay for a high free energy change [12,

13, 14]. Note however that, to be compatible with the force field of the rest of the system (i.e. ions and carbon nanotube), this latter should be polarizable as well. Some models were developed to study the influence of a local electric field on the polarization of the carbon nanotube. These models based on the numerical resolution of the Lippman-Schwinger relation were not fully implemented in the force field of molecular dynamic simulations due to the too high calculation cost [15]. The application of an external electric field would change the repartition of the local charges on all the polarizable molecules. The modified polarized dipoles could affect the resulting ionic current but are unlikely to suppress the activated behavior observed with local energy barriers.

Each carbon atom was fixed to prevent mechanical stress on the water/ion diffusion. When equilibrated, the systems were run for 5 ns before the application of a voltage ramp to study the electrical response of the infinite charged nanotube. For each electric field value, a total of 50 ns of simulation time was performed during 5 independent runs. These ensured sufficient statistics for the current evaluation. When applying the electric field, the volume of the simulations was held constant (NVT ensemble) with the cell dimensions set at the final cell dimensions of the equilibration simulations. All simulations are conducted using NAMD 2.9 [16] at a constant temperature of 300 K maintained by the Langevin dynamics method, which has been demonstrated to provide reasonable dynamics for mass transport simulations. Parameters of the simulation were chosen as following: 1fs time steps, cut-off distance of 12 Å, switching distance of 10 Å and pair list distance of 13.5 Å. Particle mesh Ewald [17] is used to calculate long-range electrostatic interactions and a Langevin piston [18] is used to maintain a pressure of 1 bar during equilibration (NPT ensemble).

The ionic current $I(t)$ was extracted from the analysis of the ionic displacement during the MD simulation using the following relation:

$$I(t) = \frac{1}{L\Delta t} \sum_{i=1}^N q_i (z_i(t + \Delta t) - z_i(t))$$

where Δt represents the time between each frame, L is the nanotube length (10 nm) and z_i the absolute position of the ion with charge q_i along the pore axis.

Statistical analysis

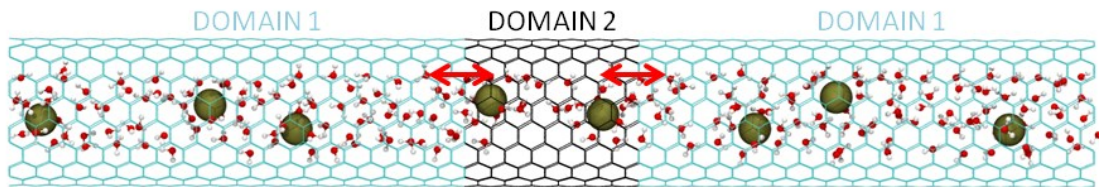


Figure S4: simulation snapshot showing the two different domains of charge in the SWCNT. Domain 1 is for the uniform charge part of the tube while domain 2 contains all the uncharged atoms of the tube. The red arrows indicate the limits between the two domains.

To analyze the role of the charge defects in the ion behavior, we calculated the average velocities of the cations inside each domain (as depicted in Fig. S4) as summarized in Table S1.

	50 mV	700 mV
DOMAIN 1	1.2 ± 0.4 m/s	38 ± 3 m/s
DOMAIN 2	5.0 ± 0.9 m/s	61 ± 8 m/s

Table S1: average velocities of ion in domains 1 and 2 during the simulations at voltage 50mV and 700mV.

The presence of a periodical charge defect inside a small nanopore decreases the average velocity of the confined particles compared to the system free of defect by a factor depending on the ion position (8 at small voltage and 4 at high voltage in domain 1, and only 2 in domain 2). The charge defect which creates an energy barrier close to $2kT$ (see figure S8) accelerates the ion by a factor a nearly 4 (2) at small voltage (high voltage, respectively). The ions, when submitted to an oriented force, do not belong to their lower energy state (the uniform negative part of the tube labeled as domain 1) when passing through the defect and diffuse rapidly to reach the opposite stable domain. Note that no significant modification of the water coordination number was observed inside each domain, confirming that the water density inside the SWCNT is enough.

The mean crossing of ions (red arrows in Fig S4) corroborates this interpretation. Indeed, at small voltage, only 42 ± 5 ions can cross the barriers while 330 ± 20 ions diffused from one side to the other at high voltage and for every 10 ns. The strong ion slow down at small voltage (compared to the free-of-defect case), partially compensated at higher voltage, is at the origin of the activated I=f(V) curves observed in the simulations.

4) Modeling of the activated I-V curves

Modeling of the activated I-V curves was performed using a model inspired by the *Butler-Volmer* model [19]. In this model, the circuit is viewed as two interfaces in series and thus the I-V equation can be written as follows:

$$I(V) = \frac{k_B T}{e} G_i \left(\exp \left[\frac{(1 - \alpha)eV}{2k_B T} \right] - \exp \left[- \frac{\alpha eV}{2k_B T} \right] \right) \quad (\text{eq. SI1})$$

where α is a dimensionless parameter accounting for the asymmetry and V is the applied voltage. As observed in figure S5, this model alone cannot account for the observed experimental data since it can correctly fit either the low voltage or high voltage regime, but not both simultaneously.

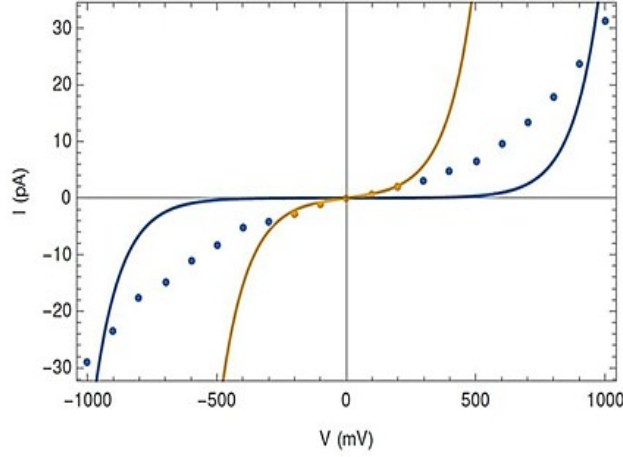


Figure S5: experimental I-V curves of device 3 fitted using the model inspired by the Butler-Volmer model.

Semi-phenomenological model

In this approach, the system is viewed as being composed of five different regions (reservoir 1, interface 1, nanopore, interface 2, and reservoir 2) contributing to the total impedance of the whole system with the interfacial impedance being dependent on the electrical potential (V) (contrary to the nanopore impedance).

At steady state, the electrical current is constant across the system. If the impedance of the two reservoirs is considered as negligible (thanks to the large aspect ratio of the nanopores), as was experimentally verified, the current I can be expressed as follows:

$$V = V_{np} + 2V_i \quad ; \quad I = G_{np}V_{np} \quad (\text{eq. SI2})$$

$$I = \frac{k_B T}{e} G_i \left(\exp \left[\frac{(1-\alpha)eV_i}{k_B T} \right] - \exp \left[-\frac{\alpha eV_i}{k_B T} \right] \right) \xrightarrow[k_B T \rightarrow 0]{eV_i} G_i V_i \quad (\text{eq. SI3})$$

where $G_{np} = \pi r_{np}^2 \kappa_{np} / L$ is the nanopore conductance, G_i is the interfacial conductance in the linear regime (*i.e.* at low voltage), and α is the asymmetry parameter. To account for symmetric I-V curves, $\alpha = 1/2$ is used since the configuration at both sides of the CNT (*i.e.* the nature of the interface and the electrolyte concentration) is considered symmetrical. The I-V curves can then be plotted using V_i as a parametric variable:

$$I(V_i) = \frac{k_B T}{e} G_i \left(\exp \left[\frac{(1-\alpha)eV_i}{k_B T} \right] - \exp \left[-\frac{\alpha eV_i}{k_B T} \right] \right) \quad (\text{eq. SI4})$$

$$V(V_i) = \frac{I(V_i)}{G_{np}} + 2V_i = \frac{k_B T}{e} \frac{G_i}{G_{np}} \left(\exp \left[\frac{(1-\alpha)eV_i}{k_B T} \right] - \exp \left[-\frac{\alpha eV_i}{k_B T} \right] \right) + 2V_i \quad (\text{eq. SI5})$$

where $k_B T = 25 \text{ meV}$ at room temperature. These equations lead to a linear response of the current at low and high voltages:

$$\frac{dI}{dV} \approx \begin{cases} \left(\frac{1}{G_{np}} + \frac{2}{G_i} \right)^{-1}, & \text{low } V \\ G_{np}, & \text{high } V \end{cases}$$

(eq. SI6)

In the intermediate voltage regime the equations can be simplified by keeping only the dominant term of the exponential contributions:

$$V = V_{np} + 2V_i \approx \frac{I}{G_{np}} + \frac{2k_B T}{e(1-\alpha)} \ln\left(\frac{eI}{k_B T G_i}\right) \quad (\text{eq. SI7})$$

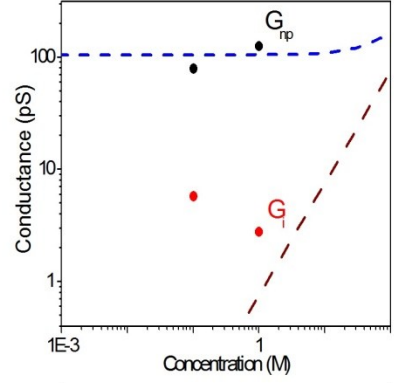
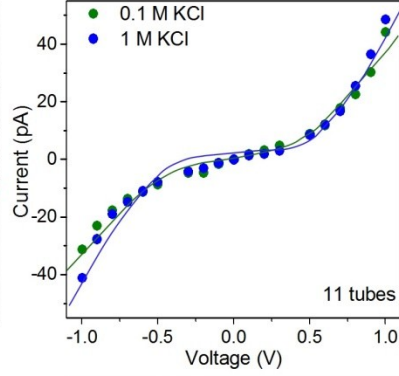
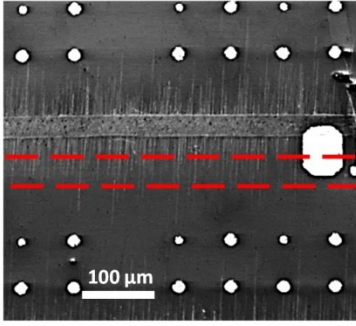
which thus gives rise to a linear “Log (I) - V” behavior when the last term in eq. 7 dominates. However, in the high voltage regime the first term dominates, giving rise to a linear “I-V” behavior. G_{np} and G_i can be used as fitting parameters to reproduce the experimental voltage-activated I-V curves.

In figure S6, the experimental voltage-activated I-V curves are fitted using equation 7. In general good agreement is observed between the semi-phenomenological modeling and the experimental data: the best agreement is found for devices 3, 4 and 5.1 while the agreement for devices 1 and 2 is fair but slightly less accurate. The G_i and G_{np} values extracted from the fits are presented as a function of the KCl concentration in Table S2.

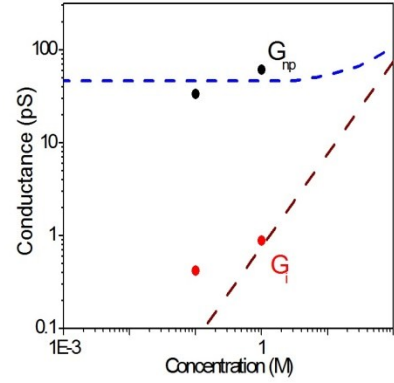
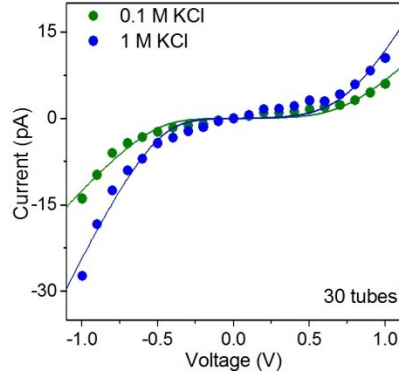
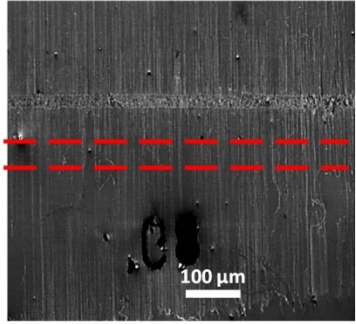
Table S2: Summary of the interfacial conductance (G_i) and nanopore conductance (G_{np}) for the different devices obtained from the fit using the developed semi-phenomenological model.

	Device 1		Device 2		Device 3			Device 4			Device 5.1		
C_{KCl} (M)	0.1	1	0.1	1	0.01	0.1	1	0.01	0.1	1	0.01	0.1	1
G_i (pS)	5.7	2.7	0.4	0.9	11.2	12.5	6.7	0.08	0.04	0.4	0.1	0.4	11.4
G_{np} (pS)	79.5	125.7	33.4	61	25.3	33	61.2	3.5	10	8.1	9.5	10.7	8.7
G_{np}/nb of tubes	7.2	11.4	1.1	2.1	8.4	11	20.4	0.15	0.4	0.4	1.2	1.4	1.1

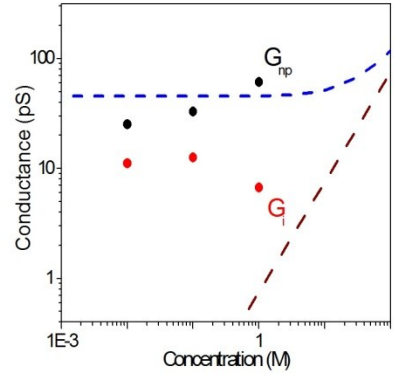
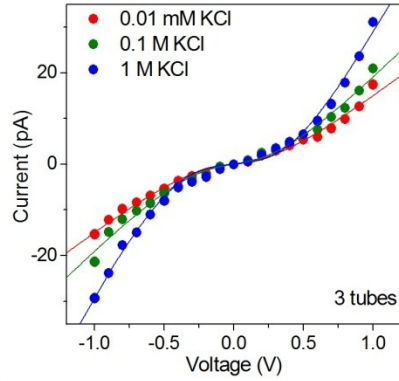
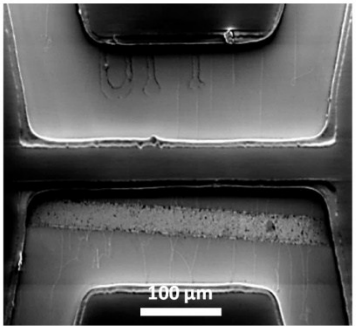
Device 1



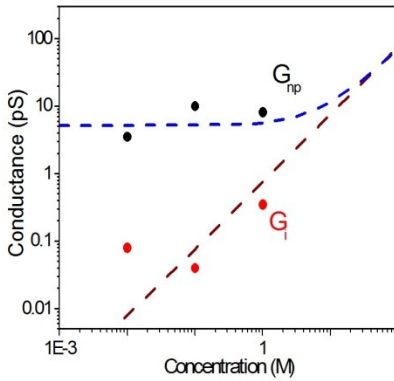
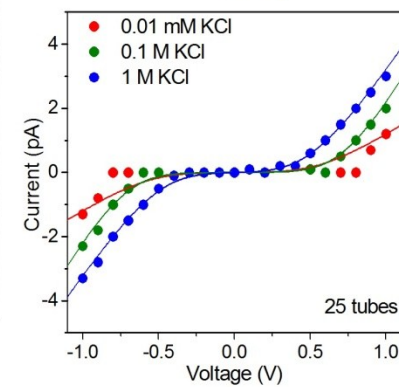
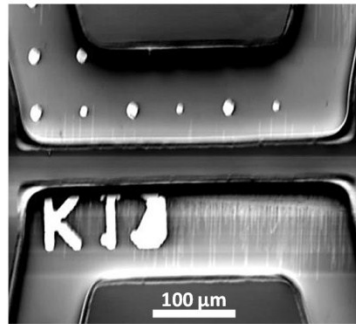
Device 2



Device 3



Device 4



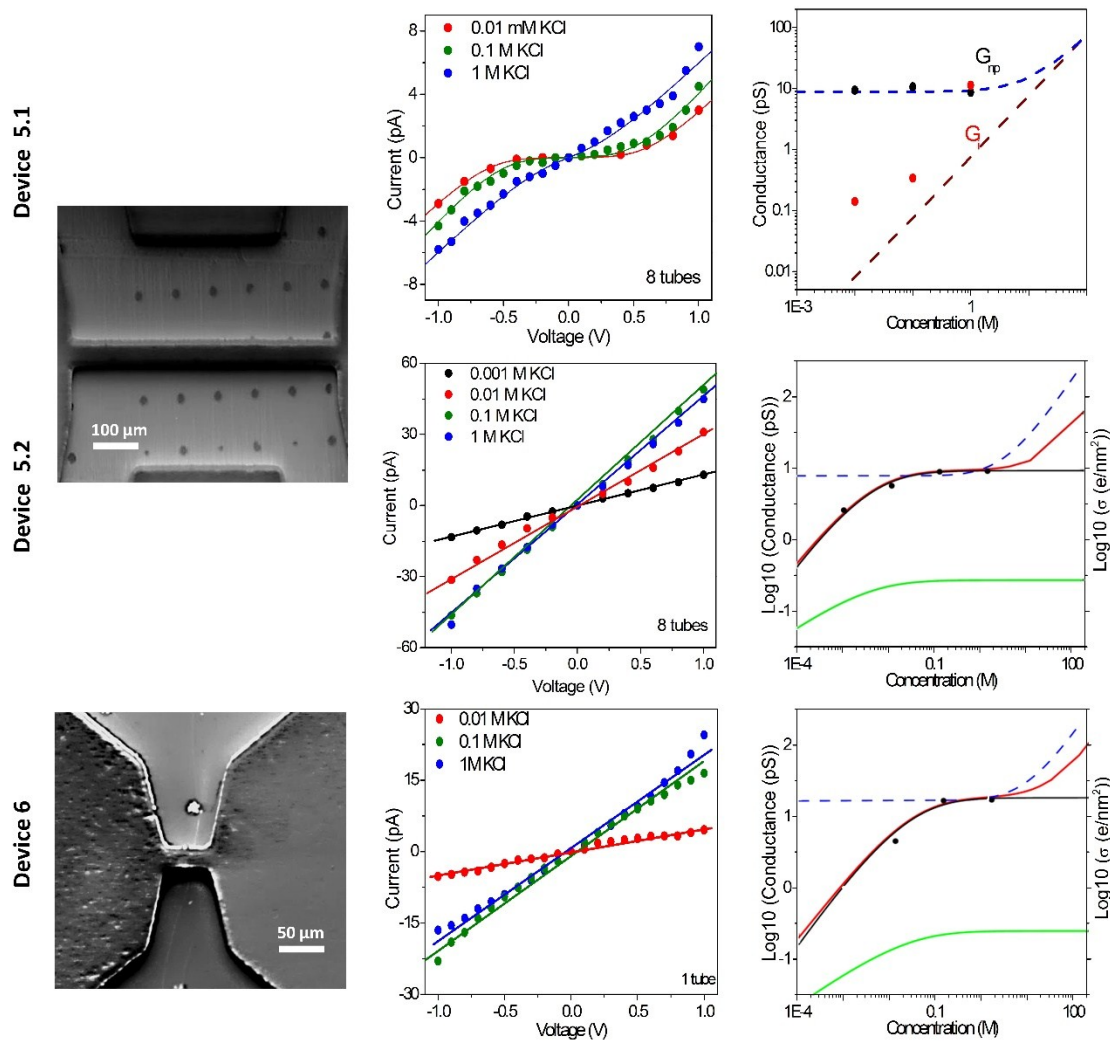


Figure S6: Summary of the experimental data (SEM, I-V and G-C) of the different characterized devices. “5.1” corresponds to the data collected for device 5 on the first day of measurements while “5.2” corresponds to the data collected for device 5 from the second day of measurements.

Fits of the conductivity of the MD simulations and experiments

We fitted the conductances measured in the MD simulations (Fig. 3 of the article) at high voltage ($V > 500$ mV) and found, for $R = 0.4$ nm and $L = 10$ nm, the following conductivities: $\kappa = 711$ S/m for the red curve without any charge defect and $\kappa = 305$ S/m for the blue curve with a defect of 0 charge over 2 nm. Knowing that the average surface charge density is $\sigma = -ne/(2\pi RL)$ where n is the number of charges on the nanopore surface ($n = 10$ without defect and $n = 8$ with the defect), one can use the formula for the nanopore conductance given in Ref. [20]:

$$G = \frac{\pi R^2}{L} \kappa \quad (\text{eq. SI8})$$

with the conductivity given by the formula in eq. SI9.

$$\kappa = e^2(\mu_+ + \mu_-)c_s \sqrt{1 + \left(\frac{\sigma}{eRc_s}\right)^2} + \frac{e|\sigma|}{R}(\mu_+ - \mu_-) + \frac{\sigma^2}{2\eta} \left[\frac{2}{\sigma^*} \left(1 - \frac{\ln(1 + \sigma^*)}{\sigma^*} \right) \right] \quad (\text{eq. SI9})$$

where e is the elementary charge, c_s is the salt concentration in the reservoirs, $\eta = 10^{-3}$ Pa.s the solvent viscosity, μ_{\pm} are the bulk mobilities of cation and anions, and b is the slip length. The normalized surface charge density σ^* is defined as

$$\sigma^* = |\sigma| \frac{\pi R l_b}{e} \quad (\text{eq. SI10})$$

where l_b is the Bjerrum length. The slip length is the only unknown parameter that we use as a fitting parameter. The fits shown in Fig. 3 of the article yield $b = 29.4$ nm for the non-defect case and $b = 19.9$ nm for the case with defect. The fact that the slip length decreases is a signature of the presence of a defect. It is important to note that Eq. (SI9) has been obtained for a homogeneously charged nanopore and that the use of this formula with a defect present is not *a priori* valid. The problem is much more involved in this case and will be treated elsewhere.

To check the value of the slip length for the non-defect case, $b = 29.4$ nm, we compare the velocity profiles obtained numerically for two different voltages $\Delta V = 50$ and 700 mV with the one obtained analytically. It is the solution of the following Stokes equation:

$$v(r) = \frac{\Delta V \epsilon}{L \eta} \left[b \frac{\partial \phi}{\partial r}(R) + \phi(R) - \phi(r) \right] \quad (\text{eq. SI11})$$

where $\phi(r)$ is the electrostatic potential in the cylindrical pore at radial distance r . Solving the Poisson-Boltzmann in the case where only counter-ions are present in the pore, as in the simulations,

one obtains, with the boundary condition $\frac{\partial \phi}{\partial r}(R) = \sigma/\epsilon$:

$$v(r) = \frac{\Delta V \sigma}{L \eta} \left[b + \frac{R}{2\sigma^*} \ln \left[1 + \sigma^* \left(1 - \left(\frac{r}{R} \right)^2 \right) \right] \right] \quad (\text{eq. SI12})$$

The velocity profile in eq. SI12 is plotted in figure S7 without a fitting parameter. One finds excellent agreement, indirectly justifying the use of eq. SI9 for the conductivity.

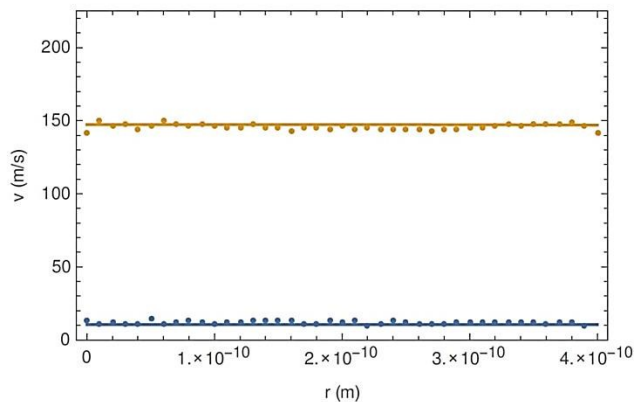


Figure S7: Water velocity profiles in the nanopore from the MD simulations for the non-defect case at two applied voltages $\Delta V = 50$ mV (blue) and 700 mV (yellow). The solid curves are Eq. (12) with no fitting parameter.

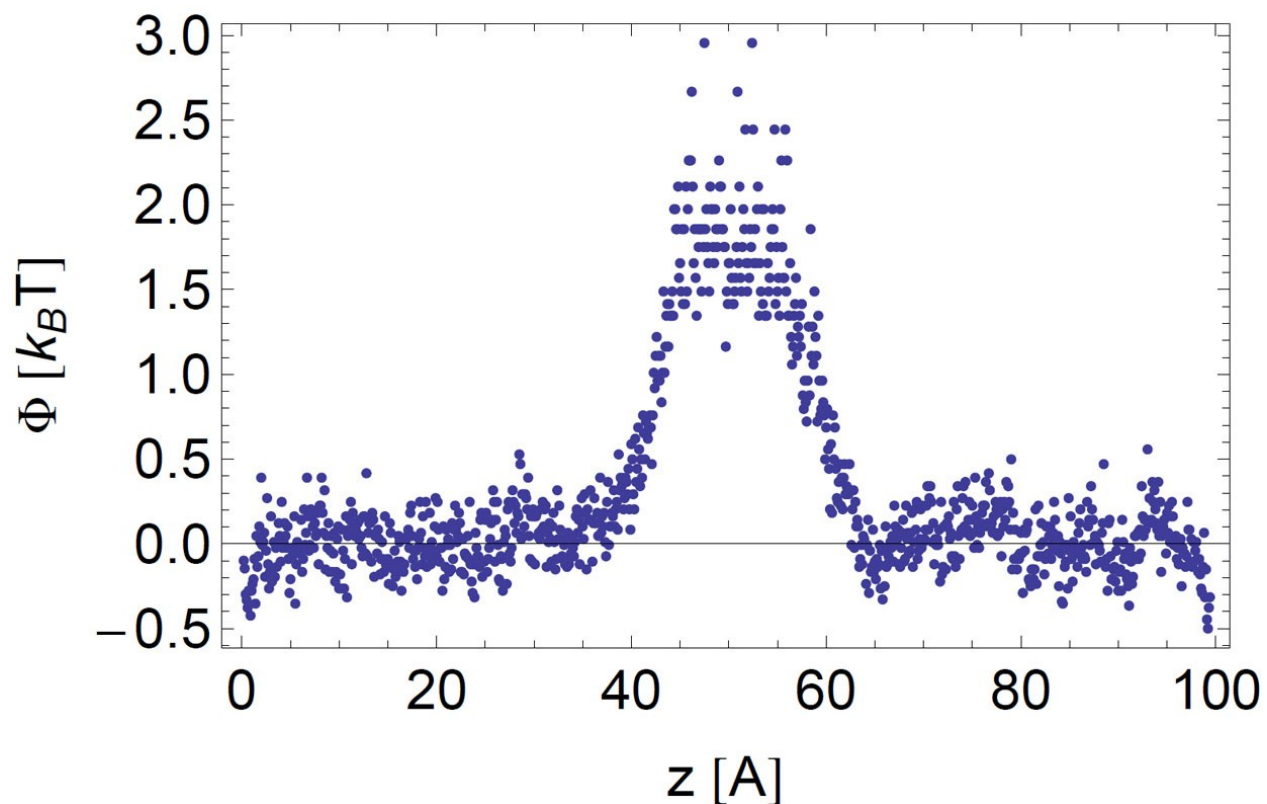


Figure S8: Potential of mean force (PMF) $\Phi(z) = -(1/kT) \ln [\rho_{ion}(z)/\rho_0]$ where $\rho_{ion}(z)$ is the ion density along the z axis of the CNT in the absence of an applied field with a 2-nm neutral section extracted from the concentration of counter-ions.

Concerning the experimental data, we fitted the conductances in Fig. 2h using the equations SI8 and SI9 for the nanopore conductance but with a surface charge density σ which is not fixed but given by the charge regulation model:

$$\sigma = \frac{\sigma_0}{1 + 10^{\frac{pK_a - pH - e\phi(R)/(k_B T)}{e}}} \quad (\text{eq. SI13})$$

with $\sigma_0 = -ne/(2\pi RL)$ where n is the number of ionizable groups on the nanopore surface, $pK_a = -\ln(K_a)$ where K_a is their dissociation constant, and $\phi(R)$ the electrostatic potential at the nanopore surface. To relate the latter to the surface charge density, we use the following interpolation formula:

$$e^{-e\phi(R)/(k_B T)} \approx \frac{\sigma^* (1 + \sigma^*)}{\pi l_B R^2 c_S} \left[\sqrt{1 + \left[\frac{\pi l_B R^2 c_S}{\sigma^* (1 + \sigma^*)} \right]^2} + 1 \right] \quad (\text{eq. SI14})$$

These two equations yield an implicit relation between σ and the salt concentration c_S , valid for the whole concentration range.

5) Additional experimental data of ion transport

Abrupt change of I-V behavior from activated to linear

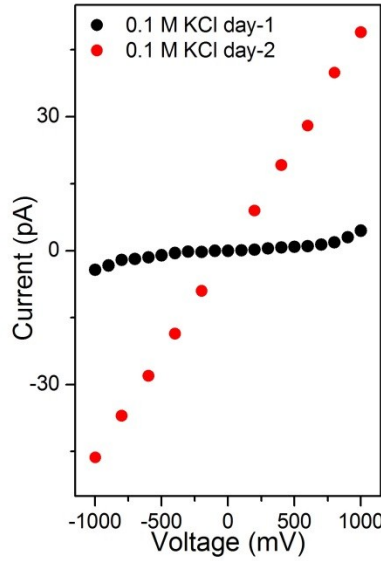


Figure S9: *I-V characteristic behavior of device 5 showing an abrupt change of I-V response from activated to linear on the second day of measurements.*

Stochastic current variations

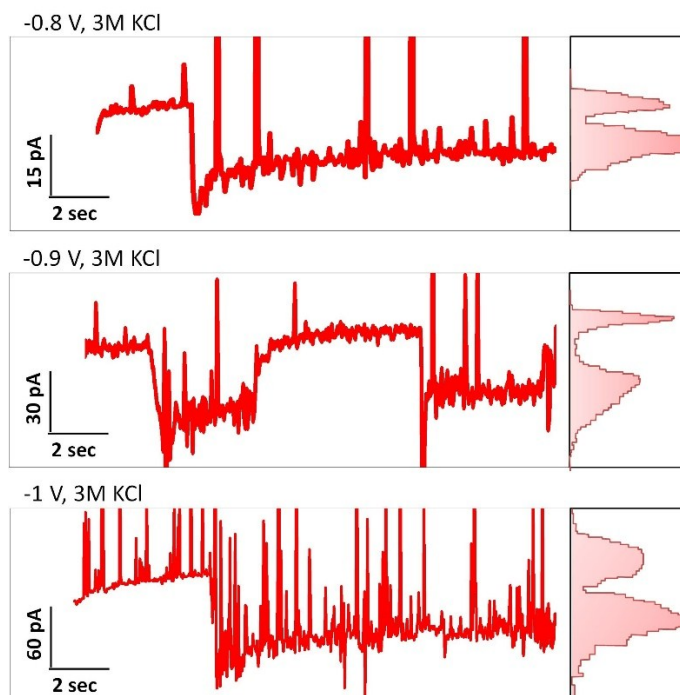


Figure S10: Typical segments of real-time current traces showing the voltage dependent variations observed in device 2 at high concentrations and voltages.

Cation selectivity

Additional cation selectivity studies were carried out for the devices that showed linear I-V behaviors (device 5.2 and 6; “5.2” corresponds to the data collected for device 5 from the second day of measurements.) using 1 M cationic chloride solutions. The obtained results, previously reported and discussed in a separate paper [21], are summarized in table S3. The ionic conductances measured for the different cations were at least one order of magnitude higher than expected from bulk electrophoretic transport and did not scale with the corresponding bulk electrophoretic mobility. This evidences a selective cation transport probably governed by a competition between steric and electrostatic effects. These results support that cations are the main charge carriers and that the SWCNT surface is negatively charged.

Table S3: Summary of the conductance (G) and normalized conductance (G/G_{bulk}) obtained for the different cations studied in two different devices (device 5.2 and 6) using 1 M electrolytes solutions.

		Li ⁺	Na ⁺	K ⁺	Cs ⁺
Device 5.2	G (pS)	17	35	40	34
	G/G _{bulk}	27	62	61	24
Device 6	G (pS)	16	28	17	-
	G/G _{bulk}	15	25	12	-

Table S4: Summary of the experimental data (I-V and G-C using KCl electrolyte, cation effect and other additional tests) of the different devices characterized.

Device summary

Device	1	2	3	4	5.1	5.2	6
Nb. of tubes	11	30	3	25	8	8	1
Kite / lattice-oriented	Lattice-oriented	Lattice-oriented	Kite	Lattice-oriented	Lattice-oriented	Lattice-oriented	Kite
Tube length (μm)	40	40	40	40	40	40	20
I-V	Voltage-activated	Voltage-activated	Voltage-activated	Voltage-activated	Voltage-activated	Linear	Linear
G-C	Weak dependence	Weak dependence	Weak dependence	Weak dependence	Sublinear	Sublinear	Sublinear
Cation selectivity	-	-	-	-	-	$\text{Li}^+ < \text{Cs}^+ < \text{K}^+ \approx \text{Na}^+$	$\text{K}^+ < \text{Li}^+ < \text{Na}^+$
I (pA) at 1 V and 1 M KCl	49	11	31	3	6	45	25
Additional Info.	-	Stochastic fluctuations at high voltages for 1 M and 3 M KCl	-	-	-	-	-

SI references

- [1] D. Zhang, J. Yang, F. Yang, R. Li, M. Li, D. Ji and Y. Li, "(n,m) Assignments and quantification for single-walled carbon nanotubes on SiO₂/Si substrates by resonant Raman spectroscopy," *Nanoscale*, vol. 7, pp. 10719-10727, 2015.
- [2] A. D. MacKerell, D. Bashford, M. Bellott, R. Dunbrack Jr., J. Evanseck, M. Field, S. Fischer, J. Gao, H. Guo, S. Ha, D. Joseph-McCarthy, L. Kuchnir, K. Kuczera, F. Lau, C. Mattos, S. Michnick, T. Ngo, D. Nguyen and B. Prodhom, "All-atom empirical potential for molecular modeling and dynamics Studies of proteins.," *Journal of Physical Chemistry B*, vol. 102, pp. 3586-3616, 1998.
- [3] W. L. Jorgensen, J. Chandrasekhar, J. D. Madura, R. W. Impey and M. L. Klein, "Comparison of simple potential functions for simulating liquid water," *J. Chem. Phys.*, vol. 79 , pp. 926-935, 1983.
- [4] S. H. Ganjiani and A. H. Nezhad, "Molecular Dynamics Simulation of the Effects of the Carbon–Water Interaction Parameters on the Nanofluidic Energy Absorption System," *Journal of Physical Chemistry C*, vol. 120, no. 22, p. 11864–11870, 2016.
- [5] L. Wang, R. S. Dumont and J. M. Dickson, "Nonequilibrium molecular dynamics simulation of water transport through carbon nanotube membranes at low pressure," *The Journal of Chemical Physics*, vol. 137, p. 044102, 2016.
- [6] N. Farhadian and M. Shariaty-Niassar, "Molecular Dynamics Simulation of Water in Single Wall Carbon Nanotube," *International Journal of Nanoscience and Nanotechnology*, vol. 5, p. 53, 2009.
- [7] J. A. Thomas and A. J. H. McGaughey, "Water Flow in Carbon Nanotubes: Transition to Subcontinuum Transport," *Physical Review Letters*, vol. 102, p. 184502, 2009.
- [8] I. L. Touriño, A. C. Naranjo, V. Negri, S. Cerdán and P. Ballesteros, "Coarse-grained molecular dynamics simulation of water diffusion in the presence of carbon nanotubes," *Journal of Molecular Graphics and Modelling*, vol. 62, pp. 69-73, 2015.
- [9] Y. Nakamura and T. Ohno, "Structure of water confined inside carbon nanotubes and water models," *Materials Chemistry and Physics*, vol. 132, p. 682– 687, 2012.
- [10] L. Liu and G. N. Patey, "Simulated conduction rates of water through a (6,6) carbon nanotube strongly depend on bulk properties of the model employed," *The Journal of Chemical Physics*, vol. 144, p. 184502, 2016.
- [11] H. Kumar, C. Dasgupta and P. K. Maiti, "Structure, dynamics and thermodynamics of single-file water under confinement: effects of polarizability of water molecules," *RSC Advances*, vol. 5, pp. 1893-1901, 2015,.
- [12] C. Bai and J. Herzfeld, "Surface Propensities of the Self-Ions of Water," *ACS Central Science*, vol. 2,

no. 4, p. 225–231, 2016.

- [13] C. D. Wick, "Hydronium Behavior at the Air–Water Interface with a Polarizable Multistate Empirical Valence Bond Model," *Journal of Physical Chemistry C*, vol. 116, no. 6, p. 4026–4038, 2012.
- [14] C. D. Wick and L. X. Dang, "Investigating Hydroxide Anion Interfacial Activity by Classical and Multistate Empirical Valence Bond Molecular Dynamics Simulations," *Journal of Physical Chemistry A*, vol. 113, no. 22, p. 6356–6364, 2009.
- [15] M. Arab, F. Picaud, M. Devel, C. Ramseyer and C. Girardet, "Molecular selectivity due to adsorption properties in nanotubes," *Physical Review B*, vol. 69, p. 165401, 2004.
- [16] J. C. Phillips, R. Braun, W. Wang, J. Gumbart, E. Tajkhorshid, E. Villa, C. Chipot, R. D. Skeel, L. Kale and K. Schulten, "Scalable molecular dynamics with NAMD," *Journal of Computational Chemistry*, vol. 26, pp. 1781-1802, 2005.
- [17] T. Darden, D. York and L. Pedersen, "Particle Mesh Ewald - an N.Log(N) Method for Ewald Sums in Large Systems.," *J Chem Phys*, vol. 98, pp. 10089-10092, 1993.
- [18] S. Feller, Y. Zhang, R. Pastor and B. Brooks, "Constant-Pressure Molecular-Dynamics Simulation - the Langevin Piston Method," *J Chem Phys*, vol. 103, pp. 4613-4621, 1995.
- [19] J. Butler, "The mechanism of overvoltage and its relation to the combination of hydrogen atoms at metal electrodes," *Transactions of the Faraday Society*, pp. 379-382, 1932 .
- [20] S. Balme, F. Picaud, M. Manghi, J. Palmeri, M. Bechelany, S. Cabello-Aguilar, A. Abou-Chaaya, P. Miele, E. Balanzat and J.-M. Janot, "Ionic transport through sub-10 nm diameter hydrophobic high-aspect ratio nanopores: experiment, theory and simulation," *Scientific Reports* 5, p. 10135, 2015.
- [21] K. Yazda, S. Tahir, T. Michel, F. Henn and V. Jourdain, "Evidence of selective cation transport through sub-2 nm single-walled carbon nanotubes," *MRS Advances*, vol. 1, p. 2079–2084, 2016.